Eur. Phys. J. E **28**, 231–242 (2009)
DOI 10.1140/epje/i2008-10388-1

THE EUROPEAN PHYSICAL JOURNAL E

Regular Article

Fluid transport at low Reynolds number with magnetically actuated artificial cilia

E.M. Gauger[1], M.T. Downton[2], and H. Stark[2,a]

[1] Department of Materials, University of Oxford, Parks Road, Oxford, OX1 3PH, UK
[2] Institut für Theoretische Physik, Technische Universität Berlin, Hardenbergstr. 36, D-10623 Berlin, Germany

Received 20 May 2008 and Received in final form 21 July 2008
Published online: 20 November 2008 –

Abstract. By numerical modeling we investigate fluid transport in low-Reynolds-number flow achieved with a special elastic filament or artifical cilium attached to a planar surface. The filament is made of superparamagnetic particles linked together by DNA double strands. An external magnetic field induces dipolar interactions between the beads of the filament which provides a convenient way of actuating the cilium in a well-controlled manner. The filament has recently been used to successfully construct the first artificial micro-swimmer (R. Dreyfus *et al.*, Nature **437**, 862 (2005)). In our numerical study we introduce a measure, which we call pumping performance, to quantify the fluid transport induced by the magnetically actuated cilium and identify an optimum stroke pattern of the filament. It consists of a slow transport stroke and a fast recovery stroke. Our detailed parameter study also reveals that for sufficiently large magnetic fields the artificial cilium is mainly governed by the Mason number that compares frictional to magnetic forces. Initial studies on multi-cilia systems show that the pumping performance is very sensitive to the imposed phase lag between neighboring cilia, *i.e.*, to the details of the initiated metachronal wave.

PACS. 87.19.rh Fluid transport and rheology – 87.16.A- Theory, modeling, and simulations – 87.16.Qp Pseudopods, lamellipods, cilia, and flagella

1 Introduction

Fluid transport and mixing on the microscopic level at low Reynolds numbers is a fascinating problem that is at the center of a successful lab-on-chip technology [1]. Nature has provided an ingenious solution to this challenge by using long elastic filaments, called flagella or cilia, that are actuated internally by molecular motors [2–4]. The resulting beating patterns, in general three-dimensional, have to be non-reciprocal as Purcell has taught us [5]. Nature uses arrays of collectively beating cilia to transport mucus in the respiratory tract, fluid in the brain [6], or to propel microorganisms such as the paramecium. During an early stage of a developing embryo, arrays of rotating cilia are responsible for establishing the left-right asymmetry in the placement of organs [7]. Recently, experimental efforts have been initiated to copy nature's successful concept by developing biomimetic or artificial cilia that are actuated by external fields [1,8,9] or to move fluid with the help of bacterial carpets [10]. On the other hand, there has been an increasing interest in recent times in contributing to the theoretical understanding of how single cilia or flagella function (*e.g.*, Refs. [11–19]) and of how their collective beating patterns, known as metachronal waves, occur (*e.g.* Refs. [12,17,20–26]).

Some years ago, Dreyfus *et al.*introduced the first artificial micro-swimmer [8] based on an artificial flagellum. This elastic filament consists of superparamagnetic micron-sized beads that are linked together by pieces of double-stranded DNA [27–29]. The flagellum is actuated by an oscillating magnetic field so that it drags an attached red-blood cell forward. Modeling using a continuum [15] or a discretized [18] approach described the behavior of the swimmer very well.

Based on our theoretical work in reference [18], we explore in this article by numerical modeling how the artificial flagellum or cilium can be employed for fluid transport. We attach the cilium to a surface and actuate it by an external magnetic field, the direction of which oscillates about the surface normal in an asymmetric fashion. To achieve fluid transport, the stroke pattern has to be asymmetric [17]. We therefore introduce a slow transport stroke, where the cilium remains nearly straight, and a fast recovery stroke, where the cilium bends due to increased hydrodynamic friction. A measure for the amount of transported fluid during one beating cycle, called pumping performance, helps us to discuss the system in detail and to identify the optimum conditions under which the

[a] e-mail: Holger.Stark@tu-berlin.de

cilium should be operated. We also look at multi-cilia systems with a defined phase lag between neighboring cilia and illustrate that such a phase lag is advantageous for fluid transport. Of course, our metachronal waves are controlled by the external field and do not occur through self-organized synchronization of the beating cilia. There is now strong evidence that this intriguing feature of biological cilia arrays is caused by hydrodynamic interactions [12,17,20–26]. Similar synchronization phenomena mediated by hydrodynamic interactions were discussed for sperm cells by Taylor [30] and for helical flagella in reference [31].

The article is organized as follows. Section 2 explains our modeling of the artificial cilium including the treatment of hydrodynamic interactions close to surfaces and the magnetic actuation cycle of the filament. Section 3 introduces the pumping performance as a measure for the transported fluid. In Sections 4 and 5 we then discuss the pumping performance for a single cilium and for multi-cilia systems. The article ends with a conclusion.

2 Model

The superparamagnetic filament is modeled by a bead-spring configuration, which additionally resists bending like a worm-like chain [32]. Consequently, each bead of the filament is subject to stretching and bending forces, for which the chemical linkers are responsible, and to dipolar interaction forces due to the induced magnetic dipoles of the beads. We completely ignore the contributions of the chemical linkers to hydrodynamic friction, so the filament interacts with the fluid surrounding solely via the hydrodynamic friction of the beads. As illustrated in Figure 1, the filament is attached to a planar surface with the help of two virtual beads that fix its position and give it an orientation orthogonal to the surface. These virtual beads contribute to elastic forces but do not participate in hydrodynamic or dipolar interactions.

In the following, we will summarize the forces, acting on each bead within the filament, and the equations of motion. Details of the derivations are given in reference [18]. The equations of motion contain hydrodynamic mobilities which we construct up to Rotne-Prager level based on the appropriate Green function commonly called Blake's tensor [33,34]. This guarantees a vanishing fluid velocity field at the bounding surface. The description of the time protocol of the actuating magnetic field concludes the section.

2.1 Energies and forces of the superparamagnetic filament

The total free energy for our bead-spring model is given by a sum over dipolar and elastic-energy contributions [18],

$$H = H^D + H^S + H^B\,, \tag{1}$$

where H^D is the dipole-dipole interaction energy, H^S is the stretching energy obeying Hooke's law and H^B is the discretized free bending energy of an elastic rod. As in our previous work, the actuation and hence also the motion of the filament takes place in the (y,z)-plane and no twisting of the filament occurs, allowing us to ignore a twisting energy in our model. We shall briefly discuss the individual energy contributions of equation (1) in the following.

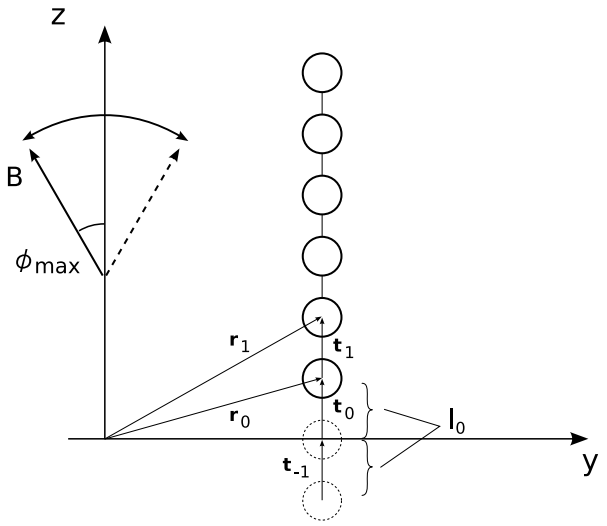

Fig. 1. Filament attached perpendicular to a bounding wall. The first three bonds $\boldsymbol{t}_{-1}$, $\boldsymbol{t}_0$ and $\boldsymbol{t}_1$ are shown. The actual filament starts with the bead at $\boldsymbol{r}_0$, whereas the virtual beads drawn as dotted lines are kept at fixed positions to anchor the filament perpendicular to the (x,y)-plane through their elastic force contributions. The actuating magnetic field oscillating around the z-axis is also sketched.

Let $\boldsymbol{t}_i$ be the vector connecting the centers of the two adjacent beads labeled i and $i-1$. A deviation $l_i = |\boldsymbol{t}_i|$ of the beads from their equilibrium spacing l_0 then gives a total stretching free energy of

$$H^S = \frac{1}{2}k\sum_{i=0}^{N-1}(l_i - l_0)^2\,, \tag{2}$$

where k is the stretching constant and N the total number of beads.

Discretizing the continuum bending energy of the worm-like chain model [32,35], we obtain by a straightforward calculation [18]

$$H^B = \frac{A}{l_0}\sum_{i=-1}^{N-2}(1 - \hat{\boldsymbol{t}}_{i+1}\cdot\hat{\boldsymbol{t}}_i), \tag{3}$$

where $\hat{\boldsymbol{t}}_i = \boldsymbol{t}_i/l_i$ and A is the bending stiffness.

Finally, consider two identical paramagnetic beads with radius a and magnetic susceptibility χ subject to a homogeneous external magnetic field $\boldsymbol{B}$. Both beads develop a dipole moment with identical orientation and strength,

$$\boldsymbol{p} = \frac{4\pi a^3}{3\mu_0}\chi\boldsymbol{B}\,, \tag{4}$$

where $\mu_0 = 4\pi\times 10^{-7}\mathrm{N/A}^2$ is the permeability of free space. The resulting dipoles of the beads of the filament

give rise to the total dipole-dipole interaction energy

$$H^D = \frac{4\pi a^6}{9\mu_0}(\chi B)^2 \sum_{i<j}^{N-1} \frac{1-3(\hat{\boldsymbol{p}}\cdot\hat{\boldsymbol{r}}_{ij})}{r_{ij}^3}\,, \tag{5}$$

where $r_{ij} = |\boldsymbol{r}_j - \boldsymbol{r}_i|$, $\hat{\boldsymbol{r}}_{ij} = (\boldsymbol{r}_j - \boldsymbol{r}_i)/r_{ij}$, and the double sum runs over all terms with $i < j$, where the minimal i is 0 and the maximal j is $N-1$.

Now that all relevant interaction energies have been characterized, the non-hydrodynamic force acting on each bead is obtained as usual,

$$\boldsymbol{F}_i = -\boldsymbol{\nabla}_{\boldsymbol{r}_i}\left(H^S + H^B + H^D\right), \tag{6}$$

where $\boldsymbol{\nabla}_{\boldsymbol{r}_i}$ is the gradient operator with respect to $\boldsymbol{r}_i$. The total non-hydrodynamic force $\boldsymbol{F}_i = \boldsymbol{F}_j^S + \boldsymbol{F}_j^B + \boldsymbol{F}_j^D$ acting on bead i is readily calculated from equations (2, 3, 5). Explicit expressions of $\boldsymbol{F}_i$ can also be found in reference [18].

2.2 Equations of motion

On the micron length scale, the motion of a particle immersed in a viscous fluid, such as water, is entirely dominated by friction and the particle's inertia can be neglected provided the time scale of interest exceeds the momentum relaxation time [36]. Hence, the velocities $\boldsymbol{v}_i$ of the beads are proportional to the forces $\boldsymbol{F}_j$ acting on them and the beads obey the following equations of motion [36]:

$$\boldsymbol{v}_i = \sum_j \boldsymbol{\mu}_{ij}\boldsymbol{F}_j\,, \quad \text{with} \quad \boldsymbol{F}_j = \boldsymbol{F}_j^S + \boldsymbol{F}_j^B + \boldsymbol{F}_j^D\,. \tag{7}$$

All the forces depend on the spatial configuration of the filament, *i.e.*, the beads' locations $\boldsymbol{r}_i$. Furthermore, the dipolar forces also possess an explicit time dependence through the external magnetic field, which we use to actuate the filament.

Hydrodynamic friction enters the equations of motion via the mobilities $\boldsymbol{\mu}_{ij}$, which depend on the geometrical configuration of the beads. The flow field induced by one moving bead creates a drag on all other beads in the vicinity and thus indirectly displaces them. Since induced flow fields are long ranged (they decay as $1/r$, where r is the distance from a moving bead), hydrodynamic interactions play an important role in viscous systems with low Reynolds number. While hydrodynamic interactions constitute a highly complicated many-body problem [36], their leading order is given by two-particle interactions. The relatively simple Rotne-Prager approximation can be employed whenever the beads are not so close together that lubrication effects need to be considered [36,37]. However, the surface, to which our filament is attached, introduces significantly more complexity due to the no-slip boundary condition even when we restrict ourselves to pairwise interactions at the Rotne-Prager level.

2.3 Hydrodynamic interactions

In the low Reynolds number regime, the fluid flow velocity at an arbitrary point $\boldsymbol{r}$ is linearly related to a point force $\boldsymbol{F}_0$ at $\boldsymbol{r}'$ by [36]

$$\boldsymbol{u}(\boldsymbol{r}) = \frac{\boldsymbol{G}(\boldsymbol{r}-\boldsymbol{r}')}{8\pi\eta}\boldsymbol{F}_0\,, \tag{8}$$

where $\boldsymbol{u}(\boldsymbol{r})$ denotes the flow field at $\boldsymbol{r}$ and η is the fluid's viscosity. In an unbounded fluid, the Green function $\boldsymbol{G}(\boldsymbol{r}-\boldsymbol{r}')$, commonly referred to as Oseen tensor in the literature, is given by

$$\boldsymbol{G}(\boldsymbol{r}) = \frac{1}{r}\boldsymbol{I} + \frac{\boldsymbol{r}\otimes\boldsymbol{r}}{r^3}\,. \tag{9}$$

Here, $\boldsymbol{I}$ is the 3×3 identity matrix and $\otimes$ denotes the dyadic product.

The aforementioned Rotne-Prager mobilities of spherical particles are commonly used quantities in an unbounded fluid, which can be derived from the Oseen tensor [36]. The respective self- and cross-mobilities are given by the following expressions for two spheres of radius a,

$$\boldsymbol{\mu}_{ii} = \mu_0\boldsymbol{I}\,, \tag{10}$$

$$\boldsymbol{\mu}_{ij}^{rp} = \mu_0\left\{\frac{3}{4}\frac{a}{r_{ij}}\left[\boldsymbol{I}+\hat{\boldsymbol{r}}_{ij}\otimes\hat{\boldsymbol{r}}_{ij}\right] + \frac{1}{2}\left(\frac{a}{r_{ij}}\right)^3\left[\boldsymbol{I}-3\,\hat{\boldsymbol{r}}_{ij}\otimes\hat{\boldsymbol{r}}_{ij}\right]\right\}, \quad i\neq j\,, \tag{11}$$

where $\boldsymbol{r}_{ij} = \boldsymbol{r}_i - \boldsymbol{r}_j$ and $\hat{\boldsymbol{r}}_{ij} = \boldsymbol{r}_{ij}/r_{ij}$ and $\mu_0 = (6\pi\eta a)^{-1}$.

However, in close proximity to a planar surface with no-slip boundary condition, the traditional Rotne-Prager mobilities can no longer be employed. The pressure and velocity fields of a point force for this boundary condition have been known for a long time and were first derived by Lorentz [40]. Blake put these results into a modern form replacing the Oseen tensor by the appropriate Green function [33]. The condition of a vanishing fluid velocity field on an infinitely extended plane is satisfied with the help of appropriate mirror images, similar to the image charge approach often used in electrostatics. In contrast to electrostatics, where it suffices to simply mirror the charge distribution, the hydrodynamic image system is more involved due to the more complicated structure of the Stokes equation when compared to the Poisson equation. Hence, so-called stresslet and source-dipole contributions are needed in addition to the stokeslet of the point force and its mirrored point disturbance (also called anti-stokeslet). This yields Blake's tensor,

$$\begin{aligned}\boldsymbol{G}^{\text{Blake}}(\boldsymbol{r},\boldsymbol{r}') &= \boldsymbol{G}(\boldsymbol{r}-\boldsymbol{r}') + \boldsymbol{G}^{im}(\boldsymbol{r},\overline{\boldsymbol{r}}')\\ &= \boldsymbol{G}(\boldsymbol{r}-\boldsymbol{r}')\\ &\quad -\boldsymbol{G}(\boldsymbol{r}-\overline{\boldsymbol{r}}') + \delta\boldsymbol{G}^{im}(\boldsymbol{r},\overline{\boldsymbol{r}}'),\end{aligned} \tag{12}$$

where $\boldsymbol{G}(\boldsymbol{r}-\boldsymbol{r}')$ and $\boldsymbol{G}(\boldsymbol{r}-\overline{\boldsymbol{r}}')$ are Oseen tensors, $\boldsymbol{r}'$ is the coordinate vector of the stokeslet source, and $\overline{\boldsymbol{r}}'$ is the position of the anti-stokeslet source, *i.e.*, the stokeslet source mirrored at the bounding (x,y)-plane $[\boldsymbol{r} = (x,y,z), \overline{\boldsymbol{r}}' = (x',y',-z')]$. Finally, $\delta\boldsymbol{G}^{im}(\boldsymbol{r},\overline{\boldsymbol{r}}')$ denotes the source-dipole and stresslet contributions.

For particles that are far apart from each other, it suffices to use the Blake tensor for the mobility functions,

i.e., to treat the particles as point-like objects, as is frequently done [23,41]. However, if the particles approach each other, their finite sizes become relevant as is the case in our filament. To take this effect into account, we derive the mobility functions in equation (7) up to the Rotne-Prager level following references [42,43]. Consider $\boldsymbol{f}(\boldsymbol{r}')$ to be the force density on the surface ∂V_j of a sphere j with its centre at $\boldsymbol{r}_j$. The force density acts on the fluid and induces the flow field

$$\boldsymbol{u}(\boldsymbol{r}) = \frac{1}{8\pi\eta}\int_{\partial V_j} \boldsymbol{G}^{\mathrm{Blake}}(\boldsymbol{r},\boldsymbol{r}')\boldsymbol{f}(\boldsymbol{r}')\,\mathrm{d}S'. \tag{13}$$

The leading order of $\boldsymbol{f}(\boldsymbol{r}')$ is $\boldsymbol{F}_j/(4\pi a^2)$, where $\boldsymbol{F}_j$ denotes the total force on particle j. Taking it into account and expanding $\boldsymbol{G}^{\mathrm{Blake}}(\boldsymbol{r},\boldsymbol{r}')$ about $\boldsymbol{r}' = \boldsymbol{r}_j$ yields for the flow field

$$\boldsymbol{u}(\boldsymbol{r}) \approx \frac{1}{8\pi\eta}\left[\left(1+\frac{a^2}{6}\boldsymbol{\nabla}^2_{\boldsymbol{r}'}\right)\boldsymbol{G}^{\mathrm{Blake}}(\boldsymbol{r},\boldsymbol{r}')\right]_{\boldsymbol{r}'=\boldsymbol{r}_j}\boldsymbol{F}_j\,. \tag{14}$$

We proceed by calculating the effect of $\boldsymbol{u}(\boldsymbol{r})$ on the motion of another sphere i with the help of Faxén's theorem [36],

$$\boldsymbol{v}_i = \frac{1}{6\pi\eta a}\boldsymbol{F}_i + \left(1+\frac{1}{6}a^2\boldsymbol{\nabla}^2_{\boldsymbol{r}_i}\right)\boldsymbol{u}(\boldsymbol{r}_i)\,. \tag{15}$$

Note that $\boldsymbol{u}(\boldsymbol{r}_i)$ also includes the flow fields created by the mirror image of sphere i, *i.e.*, by the term $\boldsymbol{G}^{im}(\boldsymbol{r},\overline{\boldsymbol{r}}')$ in the Blake tensor of equation (12). Combining equations (14) and (15), we immediately obtain the cross-mobilities [44]

$$\boldsymbol{\mu}_{ij} = \frac{1}{8\pi\eta}\left[\left(1+\frac{a^2}{6}\boldsymbol{\nabla}^2_{\boldsymbol{r}_i}\right)\left(1+\frac{a^2}{6}\boldsymbol{\nabla}^2_{\boldsymbol{r}_j}\right)\boldsymbol{G}^{\mathrm{Blake}}(\boldsymbol{r}_i,\boldsymbol{r}_j)\right], \tag{16}$$

and the self-mobility of particle i

$$\boldsymbol{\mu}_{ii} = \frac{1}{8\pi\eta}\left[\frac{4}{3a}\boldsymbol{I} + \left(1+\frac{a^2}{6}\boldsymbol{\nabla}^2_{\boldsymbol{r}_i}\right) \times \left(1+\frac{a^2}{6}\boldsymbol{\nabla}^2_{\overline{\boldsymbol{r}}_i}\right)\boldsymbol{G}^{im}(\boldsymbol{r}_i,\overline{\boldsymbol{r}}_i)\right]. \tag{17}$$

Application of the differential operators in equations (16) and (17) to the Oseen tensors $\boldsymbol{G}(\boldsymbol{r}-\boldsymbol{r}')$ and $\boldsymbol{G}(\boldsymbol{r}-\overline{\boldsymbol{r}}')$ in the Blake tensor simply gives Rotne-Prager matrices. Hence, we write the mobilities as

$$\boldsymbol{\mu}_{ii} = \mu_0\boldsymbol{I} - \boldsymbol{\mu}^{rp}(\boldsymbol{r}_i-\overline{\boldsymbol{r}}_i) + \delta\boldsymbol{\mu}_{\mathrm{self}}\,, \tag{18}$$

$$\boldsymbol{\mu}_{ij} = \boldsymbol{\mu}^{rp}(\boldsymbol{r}_i-\boldsymbol{r}_j) - \boldsymbol{\mu}^{rp}(\boldsymbol{r}_i-\overline{\boldsymbol{r}}_j) + \delta\boldsymbol{\mu}_{ij}\,, \tag{19}$$

where $\boldsymbol{\mu}^{rp}(\boldsymbol{r})$ are the Rotne-Prager tensors defined by equation (11) and $\delta\boldsymbol{\mu}_{\mathrm{self}}$ and $\delta\boldsymbol{\mu}_{ij}$ are the sourcelet and stresslet contributions originating from $\delta\boldsymbol{G}^{im}$. These evaluate to more complicated expressions which we give in Appendix B.

2.4 Reduced equations of motion

We have shown in previous work that the number of system parameters for the superparamagnetic filament can be significantly reduced by introducing just three dimensionless variables [18]. The essential parameters governing the dynamics of the filament were identified by rescaling the dynamic equations appropriately so that only reduced variables appeared. Instead of repeating the derivation of these reduced variables given in reference [18], we limit ourselves to discussing their physical significance.

One of the emerging quantities is

$$S_p = \left(\frac{6\pi\eta\frac{a}{l_0}\omega L^4}{A}\right)^{1/4} = \frac{L}{l_h}\,, \tag{20}$$

which we call "sperm number" in the following [14]. The physical interpretation of S_p is that it compares bending to frictional forces in our bead-spring chain. It bears a resemblance to a dimensionless quantity $S_p^{\perp}$ well known from analytical continuum models [11,14] when substituting $6\pi\eta a/l_0$ by $\gamma_\perp$ which is the perpendicular friction constant per unit length of a slender body. Note that $6\pi\eta a/l_0$ approximates $\gamma_\perp$ for our bead-spring chain when hydrodynamic interactions are neglected. Via $S_p = L/l_h$, one can assign a characteristic length to the system. In the continuum model of a slender body, the analogous quantity is the elastohydrodynamic penetration length $l_h^{\perp}$ [11]. An oscillation with frequency ω started at one of the ends of a sufficiently long filament penetrates the filament up to the length $l_h^{\perp}$. Conversely, if the filament is much shorter than $l_h^{\perp}$, *i.e.*, if $L \ll l_h^{\perp}$, the filament oscillates like a rigid rod over its whole length.

A second important quantity is the reduced magnetic-field strength

$$B_s = \frac{2\pi^{1/2}a^3\chi N}{3\mu_0^{1/2}l_0A^{1/2}}B\,, \tag{21}$$

which more suitably describes the effect of the external field on the superparamagnetic filament. The number B_s^2 compares dipolar to bending forces and it is proportional to the magnetoelastic number introduced in references [8,15].

Finally, we obtain a reduced spring constant

$$k_s = \frac{N^2l_0^3}{A}k\,. \tag{22}$$

While S_p and B_s are experimentally accessible via the frequency ω and the magnetic-field strength B, k_s is a fixed quantity of the superparamagnetic filament itself. Therefore, we do not make explicit use of the stretching mode of the filament and we always choose a sufficiently large k_s to keep overall length fluctuations well below 10%.

In what follows, we find that in the interesting regime for fluid transport the magnetic forces of the induced dipoles dominate over the bending forces of the superparamagnetic filament. It therefore makes sense to introduce a fourth dimensionless number as the ratio of frictional to magnetic forces. In the literature on magnetorheological suspensions, it is also called the Mason number [45,46]

$$M_a = S_p^4/B_s^2\,. \tag{23}$$

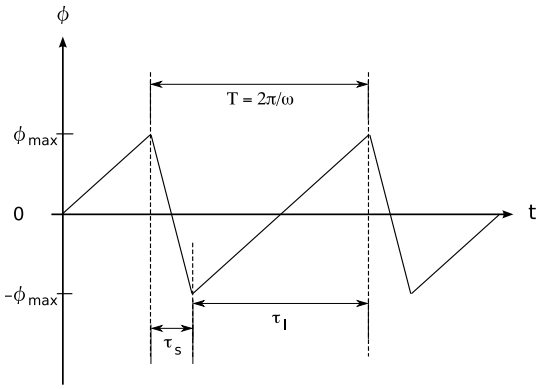

Fig. 2. The angle φ enclosed by the magnetic field $\boldsymbol{B}(t)$ and the z-axis is shown as a function of time. φ has different velocities when decreasing and increasing. The relative difference between τ_s and τ_l defines the asymmetry parameter $\varepsilon = (\tau_l - \tau_s)/(\tau_s + \tau_l)$.

2.5 Actuation of the filament

The direction of the actuating magnetic field of strength B oscillates in the (y, z)-plane (see Fig. 2)

$$\boldsymbol{B}(t) = (0, B\sin\varphi(t), B\cos\varphi(t))\,, \tag{24}$$

where $\varphi(t)$ is the angle the field encloses with the z-axis. In our modeling, the angular amplitude $\varphi_{\max}$ was always 60°. The magnetic field induces a motion of the filament caused by the time-dependent dipole-dipole interaction of the filament's constituent beads.

In order to accomplish net fluid transport, a non-reversible motion of the filament is required [5]. In addition, the motion of the filament in positive and negative y-direction has to be asymmetric to achieve fluid transport along the y-axis. In nature, the beating cycle of biological cilia can typically be broken down into a power or transport stroke, during which the cilium moves in a fashion similar to a rigid rod with high hydrodynamic resistance, and a recovery stroke, where it bends strongly and moves back with reduced resistance close to the surface. We mimic this behavior by introducing a faster stroke in one direction followed by a slower stroke back to the original position to complement the beating cycle [47]. However, in contrast to real cilia the slower stroke of our filament is the transport ("power") stroke and the faster stroke serves as the "recovery" with a bent filament. We will illustrate this below.

To accomplish the desired asymmetry, we simply rotate the $\boldsymbol{B}$ vector fast from one side to the other and move it back more slowly. Let $T = 2\pi/\omega$ be the duration of a full actuation cycle. As illustrated in Figure 2, we split T into two parts: $T = \tau_s + \tau_l$. During the fast stroke with duration τ_s, φ is decreasing with velocity $-2\varphi_{\max}/\tau_s$ and φ is increasing during the slow stroke with duration τ_l with velocity $2\varphi_{\max}/\tau_l$. To quantify the asymmetry in the actuation cycle and therefore in the beating pattern of the filament, we define the asymmetry parameter

$$\varepsilon = \frac{\tau_l - \tau_s}{\tau_s + \tau_l}\,, \tag{25}$$

which is zero for $\tau_s = \tau_l$ and tends to one in the limit of $\tau_l \gg \tau_s$.

In comparison with biological cilia or the work of Kim *et al.* [17], the magnetic actuation technique has the advantage of not requiring any active elements within the filament or its base, such as a driving motor with a geometrical switch for force reversal. Indeed, it entirely suffices to manipulate the more easily accessible macroscopic control field, whose time protocol allows us to achieve an asymmetric and non-reciprocal beating cycle.

3 Measuring the pumping performance

While a non-reciprocal and asymmetric motion of the filament is required to generate a net fluid transport, a quantity to measure the pumping performance of the filament is far from obvious. In the following we will introduce such a measure based on the works in references [17,48].

The main idea for the pumping performance is to integrate the fluid flow initiated by the beating filament over a whole plane parallel to the bounding surface. The integrated fluid flow is determined by the laterally averaged Blake tensor which assumes a particularly simple form [48]

$$\begin{aligned}\bar{G}(z,z') &= \int \mathrm{d}x\mathrm{d}y\, G_{yy}^{\mathrm{Blake}}(x,y,z,z') \\ &= \frac{z+z'-|z-z'|}{2\eta} = \frac{\min(z,z')}{\eta}\,,\end{aligned} \tag{26}$$

where we restricted ourselves to the yy component since fluid is transported along the y-direction. Then, the integrated flow $\mathcal{F}$ generated by all the beads of the filament is approximated by [49]

$$\mathcal{F}(z) = \frac{1}{2\eta}\sum_{i=0}^{N}(z + z_i - |z - z_i|)F_{yi}, \tag{27}$$

where z_i is the distance between the wall and bead i and F_{yi} is the force acting on it in the y-direction. This expression is a function of the distance z from the wall and it is constant for $z > z_i$ $(i = 1, \ldots, N)$. For our beating filament, $\mathcal{F}(z)$ changes with time but is cyclic over a full beating cycle of the filament as is illustrated in Figure 3a) for $z > L$. Figure 3b) shows $\mathcal{F}(z)$ as a function of z at different points of time during a typical beating cycle. As expected, $\mathcal{F}(z)$ only depends on z roughly over the length L of the filament and then becomes constant. Now, we consider the time average of $\mathcal{F}(z > L)$ over one beating cycle as a suitable measure for fluid transport, which we call pumping performance

$$\bar{\mathcal{F}}_\infty = \frac{1}{T}\int_t^{t+T} \mathrm{d}t'\, \mathcal{F}(z > L, t')\,, \tag{28}$$

where T is the period of one actuation cycle.

To understand how well the magnetically actuated filament transports fluid, we compare it to an idealized stroke of a rigid rod with the same length parameter $L = (N-1)l_0$ and the same thickness as the filament

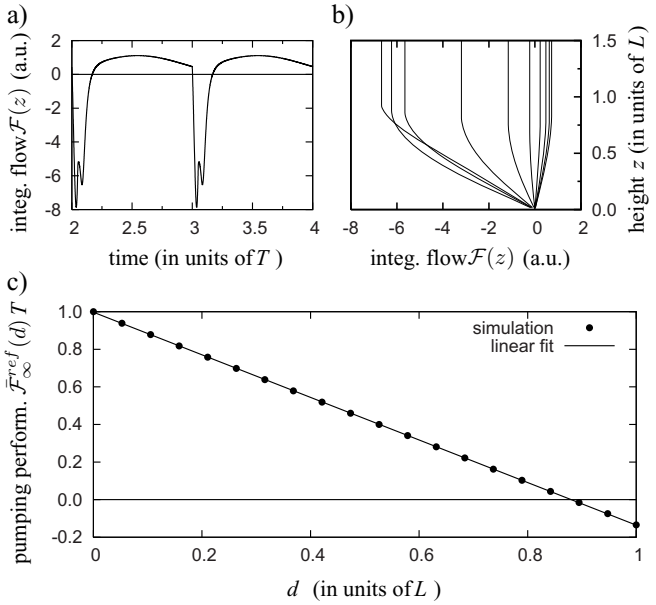

Fig. 3. a) Integrated flow $\mathcal{F}(z > L)$ in arbitrary units as a function of time in units of T for the parameters $S_p = 3$, $B_s = 3$ and $\varepsilon = 0.9$. b) Integrated flow $\mathcal{F}(z = 1.5L)$ as a function of height z at different points of time during one beating cycle. The stroboscopic snapshots to the right correspond to the slow part of the stroke and the ones to the left to the faster stroke. c) Pumping performance $\bar{\mathcal{F}}^{\mathrm{ref}}_{\infty}(0)$ times period T of the idealised reference cycle as a function of the parameter d as defined by equation (29). The y-axis is scaled to units of the maximal value $\bar{\mathcal{F}}^{\mathrm{ref}}_{\infty}(0) = 3.895 \times 10^{-14}$ m^3/s at $d = 0$.

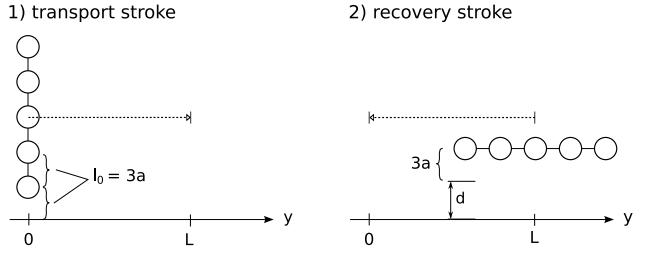

Fig. 4. Geometry of the idealized stroke of a rigid rod consisting of N particles of radius a with distance l_0 between the centers of adjacent beads. The length parameter L is defined as $L = (N-1)l_0$.

(see Fig. 4):

1) In the transport stroke the rod is oriented perpendicular to the bounding surface and it is dragged parallel to the surface along a distance L keeping its center a distance $L/2 + 3a$ above the surface.
2) The rod is then rotated by 90° to be parallel to the surface and then in the recovery stroke it is dragged along its long axis to its original position with a separation of $d + 3a$ above the surface.

In unbounded Stokes flow, the first and second part of the stroke use the respective maximal and minimal hydrodynamic resistance to produce a net fluid transport over one cycle. In the presence of a no-slip wall, the hydrodynamic resistance increases closer to the wall. Therefore, the distance d in the second part turns out to be an important parameter.

For the idealized stroke, we define a reference pumping performance

$$\bar{\mathcal{F}}^{\mathrm{ref}}_{\infty}(d) = \frac{1}{T}\int_{t}^{t+T} \mathrm{d}t'\, \mathcal{F}(z > L, t')\,, \qquad (29)$$

where $T = T_{\perp} + T_{\parallel}$ is the time required for both parts of the cycle and the variable d emphasizes the separation between the rigid rod and the surface for the second part of the reference cycle. We determined the reference pumping performance with the help of our filament as follows. We let a constant force act on each bead and numerically evaluated the average velocity of the beads in both parts of the strokes from which we then calculated the times $T_{\perp}$ and $T_{\parallel}$ the filament takes to move the length L. Together with equation (27) $\bar{\mathcal{F}}^{\mathrm{ref}}_{\infty}(d)$ is then determined. In particular, it becomes clear that $\bar{\mathcal{F}}^{\mathrm{ref}}_{\infty}(d)T$ only depends on effective friction coeffcients, L, and d. Note that in both parts of the reference stroke, the filament experiences an additional torque which alters its orientation. To really realize the idealized stroke, one would have to counterbalance the frictional torques appropriately. Figure 3c) shows $\bar{\mathcal{F}}^{\mathrm{ref}}_{\infty}(d)T$ as a function of d. A linear fit nicely connects the data points acquired by simulations and represents the linear dependence of $\mathcal{F}(z > L, t')$ on d in the recovery stroke. It makes sense that maximal pumping occurs when the recovery stroke of the reference cycle is at a minimum distance $3a$ from the wall ($d = 0$) because the no-slip boundary condition reduces the fluid volume the rod can drag along. Interestingly, a reversal of the pumping direction sets in at about $d = 0.9$. Here, the perpendicular movement of the rod gives rise to less fluid transport compared to the parallel one simply because it is on average much closer to the boundary. This highlights the importance of hydrodynamic interactions not only amongst the beads but also with the bounding wall.

The reference stroke describes an optimum fluid transport one can achieve with a rigid rod of length L close to a surface. We therefore compare the pumping performance $\bar{\mathcal{F}}_{\infty}$ of the magnetically actuated filament to the reference value $\bar{\mathcal{F}}^{\mathrm{ref}}_{\infty}(d = 0)$ at $d = 0$ *i.e.*, when the idealized reference cycle assumes ist maximum value. This results in the reduced pumping performance

$$\xi = \frac{\bar{\mathcal{F}}_{\infty}}{\bar{\mathcal{F}}^{\mathrm{ref}}_{\infty}(d = 0)}\,, \qquad (30)$$

which we use in the following. Expression $\bar{\mathcal{F}}_{\infty}$ in equation (30) is evaluated after the filament has assumed its limiting cycle, which typically happens after less than five actuation cycles after starting the simulation. We have checked that ξ evaluates to zero either if the motion of the filament is symmetric ($\tau_s = \tau_l$) or if it is reciprocal, *i.e.*, if the filament does not bend, *e.g.*, in the case

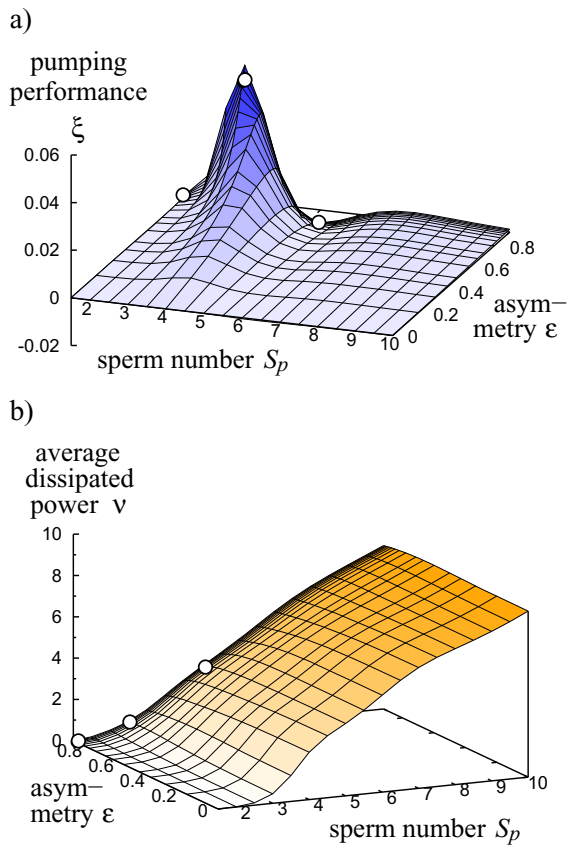

Fig. 5. Reduced pumping performance ξ (a) and the time-averaged dissipated power ν in arbitrary units (b) for a single cilium as a function of sperm number S_p and asymmetry parameter ε. The reduced magnetic-field strength is $B_s = 2.5$. The white dots mark parameters for which stroboscopic snapshots of the filament are shown in Figure 6a).

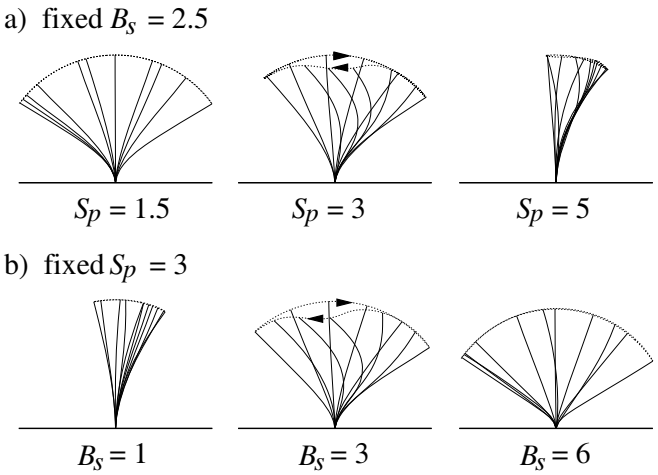

Fig. 6. Stroboscopic snapshots of the filament at different times during the beating cycle for $\varepsilon = 0.9$. The trajectory of the top bead during one beating cycle is also indicated. In the slow transport stroke the filament rotates clockwise, the fast recovery stroke occurs to the left, as indicated by the arrows. A pronounced bending of the filament occurs only at intermediate sperm number S_p and magnetic-field strength B_s.

$S_p \to 0$. Hence, equation (30) constitutes a suitable measure for characterizing the pumping performance of the magnetically actuated artificial cilium.

4 Pumping performance of a single artificial cilium

Figure 5a) shows the pumping performance ξ of a single filament as a function of the sperm number S_p and the asymmetry parameter ε at a fixed strength of the magnetic field $B_s = 2.5$. The most striking feature is that the performance is strongly peaked for ε close to one and at $S_p \approx 3$. Such a peak is also observed in the swimming velocity of the artificial micro-swimmer [8,15,18]. The corresponding stroke pattern for $S_p \approx 3$ is illustrated in the middle picture of Figure 6a). In the slow transport stroke the filament rotates clockwise being nearly straight. It uses the high friction coefficient of a rigid rod dragged perpendicular to its axis to pump fluid. In the fast recovery stroke, the filament bends due to the large hydrodynamic friction forces that scale with velocity and then relaxes back to the initial configuration. As Figure 3a) illustrates, fluid transport is also noticeable in the recovery stroke. So, the pumping performance, even for the most efficient stroke pattern, is the result of a small asymmetry in the amount of fluid transported to the right or left. In the example of Figure 3a), which is close to the optimum stroke pattern, only 4.3% of the total amount of moved fluid are effectively transported in the positive y-direction. As a result, the maximum pumping performance in Figure 5a) is only 6% of the reference stroke. As expected, the pumping performance vanishes for symmetric beating about the z-axis, *i.e.*, when $\varepsilon = 0$. The same is true for $S_p \to 0$: The filament follows the actuating magnetic field instantaneously. Aside from the base, the filament therefore remains straight and the stroke is reciprocal. The left picture in Figure 6a) gives an example of such a stroke. A reversal of the pumping direction ($\xi < 0$) occurs at $S_p \approx 5.5$, albeit only with a rather weak performance. Finally, the pumping performance goes to zero for increasing S_p or frequency since the filament can no longer follow the actuating field as illustrated in the right picture of Figure 6a). In summary, an optimal pumping performances is only achieved for intermediate values of S_p.

Let us add a further remark. Naively, one might anticipate that the closer ε is to one, the more pronounced the incurred bending during the fast part of the actuation cycle, giving rise to better pumping performance. However, a limit on the maximal speed with which the filament manages to follow the field exists. The extreme case of instantaneous switching of the direction of the magnetic field in the recovery stroke ($\tau_s = 0$) is not conducive to generating fluid transport. On the contrary, it seems important that the free end of the filament follows the magnetic field's orientation during the fast stroke. Relaxation from the bent

to a straight configuration then happens during the time interval τ_l allotted to the slow part of the cycle. Consequently, the filament takes significantly longer to perform the actual recovery stroke of the cycle than the magnetic field. Naturally, this observation translates into the fact that the ε value at which maximum pumping performance occurs decreases with increasing S_p. In Figure 5a), where ε ranges up to 0.94 this is visible to the right of the optimal pumping performance.

Part b) of Figure 5 shows the time average of the dissipated power

$$\nu = \frac{1}{T}\int_t^{t+T} \sum_{i=0}^{N} \boldsymbol{v}_i \cdot \boldsymbol{F}_i \mathrm{d}t' \,, \tag{31}$$

as a function of S_p and ε. Surprisingly, it does not display such a pronounced behavior as the pumping performance. Particularly, there is hardly any dependence on the asymmetry parameter ε visible. Being proportional to the square of the beads' velocities, one could assume $\nu \sim \omega^2$ and therefore $\nu \sim S_p^8$ (recall that $S_p \sim \omega^{1/4}$). At small S_p, the data shown in Figure 5b) do show a steep incline. However, they do not increase as S_p^8, because already at S_p around 2 the filament does not completely follow the actuating field as the snaphots in Figure 6a) illustrate. This effect becomes more pronounced for increasing S_p, and the data clearly deviate from the naive assumption of $\nu \sim S_p^8$. The third picture in Figure 6a) demonstrates that already at $S_p = 5$ the filament lags significantly behind the actuating magnetic field.

As illustrated by the three-dimensional plot of Figure 7a), there exists a pronounced dependence of the pumping performance ξ on the strength B_s of the actuating magnetic field which has also been observed in the swimming velocity of the artificial micro-swimmer [8,15, 18]. Figure 7b) shows this behavior for different constant values of S_p. Increasing the magnetic field from zero, the pumping perfomance stays close to zero and then, beyond a certain threshold value, it grows until it reaches a maximum. It finally decreases and even becomes negative. The snapshots in Figure 6b) again explain this behavior. Small field strengths B_s are not high enough to overcome the hydrodynamic friction forces and therefore the motion of the filament is very limited. On the other hand, at large strengths B_s the filament is always straight and therefore performs a reciprocal motion. An optimal stroke only exists in an intermediate regime for the strength B_s. Clearly, the optimal performance shifts with increasing S_p to larger values of B_s since a larger field is needed to move the filament through the fluid. In other words, for larger B_s the filament is stiffer and a higher frequency $\omega \propto S_p^4$ is needed to achieve the optimum stroke. Higher frequency means larger frictional forces and therefore a larger pumping performance, as Figures 7a) and b) demonstrate. When the magnetic forces on the filament exceed the bending forces, one expects the dynamics of the filament to be determined by the ratio of the hydrodynamic friction to magnetic forces, which we introduced in equation (23) as Mason number M_a. From Figure 7a) we extract curves $\xi(S_p)$ for different constant B_s and rescale each of these curves with

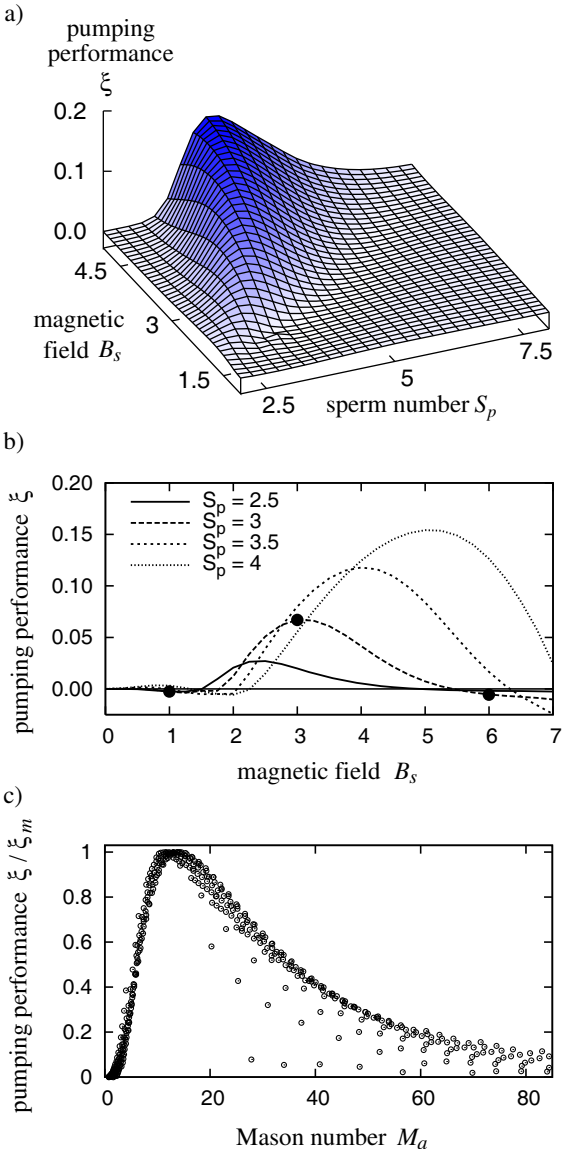

Fig. 7. a) Pumping performance ξ as a function of S_p and B_s for $\varepsilon = 0.9$. b) Plot of ξ *versus* B_s for different S_p. The black dots mark parameters for which stroboscopic snapshots of the filament are shown in Figure 6b). c) Pumping performance ξ as a function of the Mason number $M_a = S_p^4/B_s^2$, where ξ is given in units of the maximum values ξ_m when B_s is kept constant.

the respective maximum values ξ_m. In Figure 7c), all the data points for $B_s \geq 2$ are plotted as a function of the Mason number M_a. Indeed, most of the data points fall on a master curve, as predicted. Deviations occur for data points with B_s close to 2.

5 Pumping performance of hydrodynamically interacting cilia

Nature often uses arrays of beating cilia rather than a single isolated cilium for generating fluid transport or to propel microorganisms such as a paramecium [2]. These

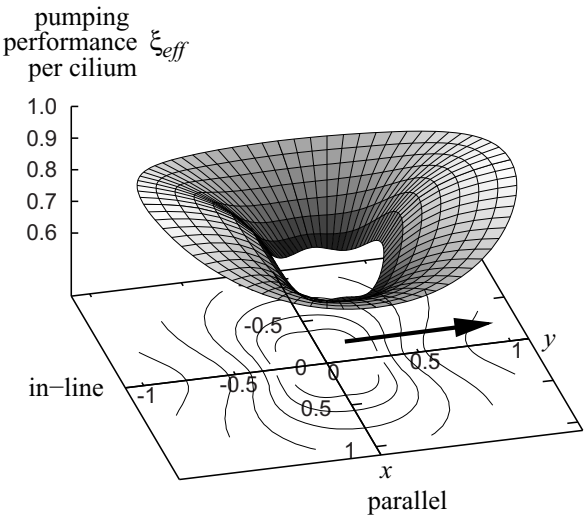

Fig. 8. Effective pumping performance ξ_{eff} for a two-cilia system. One cilium is placed at $x = y = 0$, the other cilium at different points in the (x, y)-plane with coordinates in units of L. The effective pumping performance per cilium, ξ_{eff}, is given in units of the performance ξ for a single, unperturbed filament actuated with the same parameters $S_p = 3$, $B_s = 3$ and $\varepsilon = 0.9$. The base contour lines run from 0.4 (innermost) to 0.9 (outermost) in steps of 0.1. The arrow indicates the pumping direction along the y-axis.

cilia beat in a synchronized fashion with a defined phase difference giving rise to so-called metachronal waves. As reviewed in the introduction, analytical and numerical investigations of beating cilia suggest that hydrodynamic interactions between single cilia synchronize their beating by inducing such a phase lag and therefore waves to occur. For example, in reference [17] model cilia are driven by imposing a torque at the base of each cilium. This torque is reversed once the angular amplitude of the cilium close to the base exceeds a certain threshold value. Due to this mechanism, the phase of the driving torque and therefore of each cilium can change during the beating cycle and a phase lag between neighboring cilia can evolve. This cannot happen for the magnetically actuated cilia studied in this paper since the oscillating magnetic field determines the phase of each cilium. Nevertheless, one might ask if in our system the zero-phase-lag state is stable. We have never observed an instability towards a state with non-zero phase lag. This seems to be reasonable: the actuating magnetic field ultimately determines the forces which drive the filament against the hydrodynamic friction through the liquid. Since these forces are much larger than the hydrodynamic interactions between the cilia, a noticable phase lag between the cilia cannot occur. On the other hand, the artificial cilia system can be used to investigate in a systematic way how the pumping performance depends on the phase lag between the cilia by actuating each cilium with a separate magnetic field. In the following, we present initial results of such a study.

In Figure 8 we first investigate the pumping performance of a two-cilia system with zero phase lag between the cilia. One cilium is placed at the center $x = y = 0$ and the other at different points in the (x, y)-plane. We introduce an effective pumping performance per cilium, ξ_{eff}, in units of the performance ξ of a single cilium actuated with the same magnetic-field cycle. If the cilia are sufficiently well separated from each other, ξ_{eff} approaches the pumping performance of a single filament, as expected. If the cilia approach each other, ξ_{eff} decreases. Due to hydrodynamic interactions between the cilia beating with the same phase, their effective friction with the surrounding fluid is reduced and therefore they pump less fluid. Figure 8 clearly shows that this effect is more pronounced in the parallel configuration, where the cilia are placed next to each other on the x-axis while the strokes are performed in the (y, z)-plane. On the other hand, in the in-line configuration, where the cilia sit behind each other on the y-axis, ξ_{eff} has almost reached the single-cilium performance ξ at a distance L.

Next we study the pumping performance and the dissipated energy of several cilia placed on the y-axis in the in-line configuration. Neighboring cilia are actuated by different magnetic fields with a prescribed phase shift $\Delta\varphi$. As illustrated by the first row in Figure 10a), a cilium lags behind its neighboring cilium to the left by the small phase shift $\Delta\varphi$. Note that the slow transport stroke with a straight cilium goes to the right as can be seen from the snapshots at different times in Figure 10a). Furthermore, when time proceeds, the strongly bent cilium in the recovery stroke also moves to the right. So metachronal wave propagation and transport stroke occur in the same direction which is also termed symplectic metachronism in the literature [2]. However, note that in biological systems the transport stroke is faster than the recovery stroke. On the other hand, for phase shifts close to 2π (see Fig. 10b)) a cilium moves ahead of its neighbor to the left. As a result, the metachronal wave propagates opposite to the transport stroke and is therefore termed antiplectic. Figure 9a) demonstrates that the average effective pumping performance per cilium, ξ_{eff}, falls below the reference value of a single cilium for small $\Delta\varphi$, while it assumes a maximum value at around $\Delta\varphi = 0.8 \times 2\pi$, *i.e.*, in the antiplectic mode. The maximal pumping performance ξ_{eff} increases with the number of cilia and slightly moves to larger $\Delta\varphi$. Even at the relatively large distance of $1.5L$ between the cilia, ξ_{eff} is increased by more than 40% relative to a single cilium. Preliminary calculations show that this value strongly increases, when the cilia are moved closer together. Hence, our study clearly demonstrates that metachronal coordination of ciliary beating at the right phase shift significantly enhances the ability to transport fluid. An explanation for this behavior can be inferred from the snapshots in Figure 10. In the optimum stroke (see Fig. 10b)), the fifth cilium from left performs the recovery stroke against the neighboring fourth cilium which hinders the fluid flow initiated by recovery stroke and therefore increases fluid transport to the right. On the other hand, in the metachronal wave with lowest pumping performance (see Fig. 10a)), the cilium performing the recovery stroke is further away from the neighboring cilia and therefore its

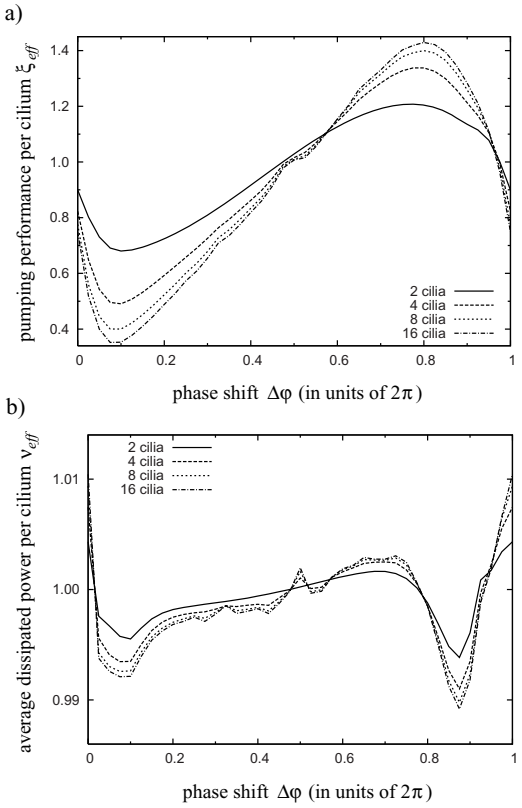

Fig. 9. a) Average effective pumping performance ξ_{eff} for multi-cilia systems in the in-line configuration as a function of the phase shift between neighboring cilia. ξ_{eff} is given in units of the performance ξ for a single, unperturbed filament actuated with the same parameters $S_p = 3$, $B_s = 3$ and $\varepsilon = 0.9$. b) Average dissipated power ν_{eff} for multi-cilia systems in the in-line configuration as a function of the phase shift between neighboring cilia. ν_{eff} is given in units of the dissipated power ν for a single, unperturbed filament.

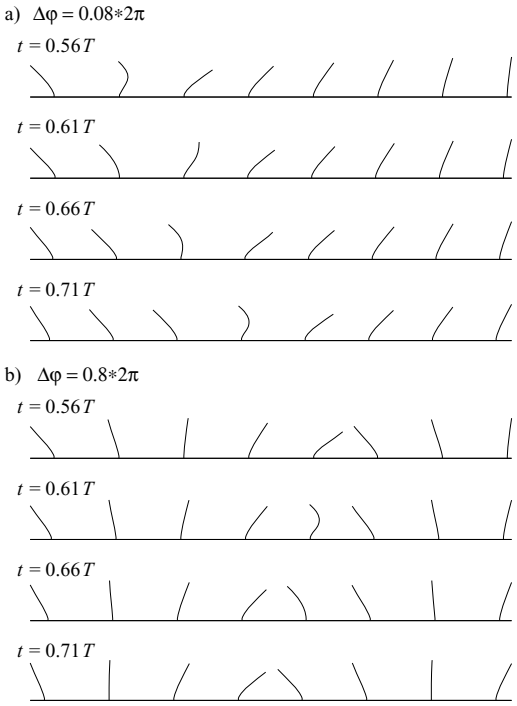

Fig. 10. Snapshots of the in-line configuration with eight cilia for different phase shifts: a) $\Delta\varphi = 0.08 \times 2\pi$ (minimal pumping performance) and b) $\Delta\varphi = 0.8 \times 2\pi$ (optimum pumping performance). The times given in units of the time period T belong to the field cycle of the rightmost cilium.

fluid transport is hardly hindered. While the pumping performance is strongly influenced by the phase shift and the number of beating cilia, the average dissipated power per cilium, ν_{eff}, only exhibits very weak dependence on these parameters. As illustrated in Figure 9b), ν_{eff} deviates from the single-cilium value by at most 1%. This is in contrast to the work of Gueron and Levit-Gurevich, who, *e.g.*, found that for a 10-cilia system with a distance of $0.7L$ between the cilia ν_{eff} decreases by ca. 40% relative to the value of a single cilium [21]. We checked that the smaller distance is not the major reason for this difference. It might be due to the fact that these authors model biological cilia with their internal actuation mechanism, whereas our cilia are actuated by an external field.

6 Conclusion

We have performed a thorough theoretical investigation of a magnetically powered low-Reynolds-number pumping device. It consists of a superparamagnetic elastic filament that is attached to a surface and that can be conveniently actuated by an external magnetic field. We have introduced a reduced pumping performance ξ that quantifies the fluid transport and compares it to the value of an idealized transport stroke of a rigid rod. With the help of ξ, we have identified an optimum stroke pattern of the magnetically actuated artificial cilium. It consists of a slow transport stroke and a fast recovery stroke in contrast to nature. Our detailed parameter study for the reduced magnetic field B_s and the sperm number S_p reveals that for sufficiently large B_s the behavior of the artificial cilium is mainly governed by the Mason number that compares frictional to magnetic forces. Initial studies on multi-cilia systems reveal that the pumping performance is very sensitive to the imposed phase lag between neighboring cilia, *i.e.*, to the details of the initiated metachronal waves. Due to our results, we expect that metachronal waves in real cilia systems also increase the pumping performance for fluid transport.

Experiments using the superparamagnetic elastic filament for fluid transport are currently under way [50]. Our study will help to identify relevant parameter ranges in which the artifical cilium can be operated optimally. Initiating metachronal waves in the multi-cilia system will be important for increasing the pumping performance. This requires oscillating magnetic fields, the phases of which should vary from one cilium to the other. The realization of such a system is not unrealistic [51] but certainly poses a challenge to experimentalists. It would help to establish the artificial cilium as a useful tool for fluid transport in microfluidic devices.

Table 1. Parameters used in the numerical studies.

Parameter	Simulation value
N	20
a (μm)	0.5
l_0	$3a$
$\rightarrow L$ (μm)	28.5
χ	0.993
η (N s/m^2)	10^{-3}
k (N/m)	$1.5 \cdot 10^{-3}$
A (N m)	$4.5 \cdot 10^{-22}$
ω ($2\pi/s$)	0.071–140.72
$\rightarrow S_p$	1.5–10
B (T)	0–0.085
$\rightarrow B_s$	0–7
$\varphi_{\max}$ (degrees)	60
Δt (s)	$\mathcal{O}(10^{-6})$
n_s	≈ 5

The authors would like to thank J. Bibette, R. Dreyfus, M. Fermigier, G. Maret, M. Reichert, and H. Stone for engaging and interesting discussions. EMG and HS thank the International Graduate College at the University of Konstanz for financial support and the MPI for Dynamics and Self-Organization in Göttingen for providing us with computing time. EMG acknowledges support from the Marie Curie Early Stage Training network QIPEST (MEST-CT-2005-020505). MD and HS acknowledge financial support from the Deutsche Forschungsgemeinschaft under Grant No. Sta 352/7-1.

Appendix A. Simulation parameters

In Table 1, we summarize the parameters used for the numerical simulations. The oscillation frequency $\omega = 2\pi/T$ and the magnetic-field strength B were varied to study the respective ranges of sperm number S_p and reduced magnetic field B_s. The spring constant k, the time step Δt for the Euler integration, and the number n_s of simulation cycles were adjusted as necessary. Typical values are shown.

Appendix B. Mobilities

Explicit expressions for the stresslet and sourcelet contributions of Blake's tensor can be calculated from reference [33] or taken directly from reference [52]. Starting with these, we have calculated the self- and cross-mobilities as outlined in the main text.

Appendix B.1. Self-mobilities

Due to the axial symmetry of the sphere with its image system, all but the diagonal elements vanish and the xx and the yy elements are identical:

$$\delta\boldsymbol{\mu}_{\text{self}} = \frac{1}{6\pi\eta a}\begin{pmatrix}\nu & 0 & 0\\ 0 & \nu & 0\\ 0 & 0 & 2\nu\end{pmatrix}, \tag{B.1}$$

where ν is given by (with a being the radius of the bead and z the distance to the plane)

$$\nu = -\frac{3}{16}\left[\frac{a}{z} - \left(\frac{a}{z}\right)^3 + \frac{1}{3}\left(\frac{a}{z}\right)^5\right]. \tag{B.2}$$

Once the expression above is included into formula (18) for $\boldsymbol{\mu}_{ii}$, the self-mobility agrees with the expression given in reference [41].

Appendix B.2. Cross-mobilities

Symmetry dictates that the xy and yx elements are identical (the boundary wall is in the (x, y)-plane). Furthermore, the xx and yy elements are formally equivalent when R_x is interchanged with R_y. The same holds for the xz and yz or zx and zy elements, respectively.

The positions of the beads are $\boldsymbol{r}_1 = (x_1, y_1, z_1)$ and $\boldsymbol{r}_2 = (x_2, y_2, z_2)$ and the image system is located at $\overline{\boldsymbol{r}}_2 = (x_2, y_2, -z_2)$. Furthermore, for convenience we define $s = |\boldsymbol{r}_1 - \overline{\boldsymbol{r}}_2|$ and $R_x = (x_1 - x_2)$, $R_y = (y_1 - y_2)$ and $R_z = (z_1 + z_2)$. Let α and β refer to the x and y but not the z coordinate. In this notation, we obtain the following components for the cross-mobilities:

$$\begin{aligned}(\delta\boldsymbol{\mu}_{12})_{\alpha\alpha} = \frac{1}{4\pi\eta}\Bigg[&- z_1 z_2\left(\frac{1}{s^3} - 3\frac{R_\alpha^2}{s^5}\right)\\ &-\frac{a^2}{s^7}R_z^2\left(4R_\alpha^2 - R_\beta^2 - R_z^2\right) - \frac{a^4}{3s^9}\left(4R_\alpha^4 - R_\beta^4\right.\\ &\left.+4R_z^4+3R_\alpha^2R_\beta^2+3R_\beta^2R_z^2-27R_\alpha^2R_z^2\right)\Bigg],\end{aligned} \tag{B.3}$$

$$\begin{aligned}(\delta\boldsymbol{\mu}_{12})_{zz} = \frac{1}{4\pi\eta}\Bigg[&z_1 z_2\left(\frac{1}{s^3} - 3\frac{R_z^2}{s^5}\right)\\ &-\frac{a^2}{s^7}R_z^2\left(3(R_\alpha^2 + R_\beta^2) - 2R_z^2\right)\\ &-\frac{a^4}{3s^9}\left(3R_\alpha^4 + 3R_\beta^4 + 6R_\alpha^2R_\beta^2\right.\\ &\left.-24R_z^2(R_\alpha^2 + R_\beta^2) + 8R_z^4\right)\Bigg],\end{aligned} \tag{B.4}$$

$$\begin{aligned}(\delta\boldsymbol{\mu}_{12})_{\alpha\beta} = \frac{1}{4\pi\eta}\Bigg[&\frac{3z_1z_2R_\alpha R_\beta}{s^5} - \frac{5a^2}{s^7}R_\alpha R_\beta R_z^2\\ &-\frac{5a^4}{3s^9}\left(R_\alpha^2 + R_\beta^2 - 6R_z^2\right)R_\alpha R_\beta\Bigg],\end{aligned} \tag{B.5}$$

$$(\delta\boldsymbol{\mu}_{12})_{\alpha z} = \frac{1}{4\pi\eta}\Bigg[R_\alpha\left(\frac{{z_1}^2}{s^3} - 3\frac{z_1 z_2 R_z}{s^5}\right) + R_\alpha a^2\left(\frac{1}{3}\frac{1}{s^3} + \frac{5}{s^7}R_z^3 - \frac{1}{s^5}\left[R_z + 2(z_1^2 + z_1 z_2)\right]\right) + \frac{5a^4}{3s^9}R_\alpha(3R_z[R_\alpha^2 + R_\beta^2] - 4R_z^3)\Bigg], \quad \text{(B.6)}$$

$$(\delta\boldsymbol{\mu}_{12})_{z\alpha} = \frac{1}{4\pi\eta}\Bigg[R_\alpha\left(\frac{{z_1}^2}{s^3} + 3\frac{z_1 z_2 R_z}{s^5}\right) + R_\alpha a^2\left(\frac{1}{3}\frac{1}{s^3} - \frac{5}{s^7}R_z^3 + \frac{1}{s^5}\left[R_z - 2(z_1^2 + z_1 z_2)\right]\right) - \frac{5a^4}{3s^9}R_\alpha(3R_z[R_\alpha^2 + R_\beta^2] - 4R_z^3)\Bigg]. \quad \text{(B.7)}$$

References

1. J. den Toonder, F. Bos, D. Broer, L. Filippini, M. Gillies, J. de Groede, T. Mol, M. Reijme, W. Talen, H. Wilderbeek, V. Khatavkar, P. Anderson, Lab Chip **8**, 533 (2008).
2. C. Brennen, H. Winet, Annu. Rev. Fluid Mech. **9**, 339 (1977).
3. R.W. Linck, *Cilia and Flagella*, in *Encyclopedia of Life Sciences* (Wiley, Chichester, 2001), `www.els.net`.
4. D. Bray, *Cell Movements: From Molecules to Motiliy*, 2nd edition (Garland Publishing, New York, 2001).
5. E.M. Purcell, Am. J. Phys. **45**, 3 (1977).
6. I. Ibañez-Tallon, A. Pagenstecher, M. Fliegauf, H. Olbrich, A. Kispert, U.-P. Ketelsen, A. North, N. Heintz, H. Omran, Hum. Mol. Genet. **13**, 2133 (2004).
7. C.D. Stern, Nature **418**, 29 (2002); J.J. Essner, K.J. Vogan, M.K. Wagner, C.J. Tabin, H.J. Jost Yost, M. Brueckner, Nature **418**, 37 (2002); S. Nonaka, H. Shiratori, Y. Saijoh, H. Hamada, Nature **418**, 96 (2002).
8. R. Dreyfus, J. Baudry, M.L. Roper, M. Fermigier, H.A. Stone, J. Bibette, Nature **437**, 862 (2005).
9. B.A. Evans, A.R. Shields, R. Lloyd Carroll, S. Washburn, M.R. Falvo, R. Superfine, Nano Lett. **7**, 1428 (2007).
10. N. Darnton, L. Turner, K. Breuer, H.C. Berg, Biophys. J. **86**, 1863 (2004).
11. C.H. Wiggins, R.E. Goldstein, Phys. Rev. Lett. **80**, 3879 (1998); C.H. Wiggins, D. Riveline, A. Ott, R.E. Goldstein, Biophys. J. **74**, 1043 (1998).
12. S. Gueron, K. Levit-Gurevich, Biophys. J. **74**, 1658 (1998).
13. S. Camalet, F. Jülicher, J. Prost, Phys. Rev. Lett. **82**, 1592 (1999); S. Camalet, F. Jülicher, New J. Phys. **2**, 24 (2000).
14. C.P. Lowe, Philos. Trans. R. Soc. London, Ser. B **358**, 1543 (2003); M.C. Lagomarsino, F. Capuani, C.P. Lowe, J. Theor. Biol. **222**, 215 (2003).
15. M.L. Roper, R. Dreyfus, J. Baudry, M. Fermigier, J. Bibette, H.A. Stone, J. Fluid Mech. **554**, 167 (2006); Proc. R. Soc. London, Ser. A **464**, 877 (2008).
16. M. Manghi, X. Schlagberger, R. Netz, Phys. Rev. Lett. **96**, 068101 (2006).
17. Y. Kim, R. Netz, Phys. Rev. Lett. **96**, 158101 (2006).
18. E. Gauger, H. Stark, Phys. Rev. E **74**, 021907 (2006).
19. E. Lauga, Phys. Rev. E **75**, 041916 (2007).
20. S. Gueron, K. Levit-Gurevich, N. Liron, J.J. Blum, Proc. Natl. Acad. Sci. U.S.A. **94**, 6001 (1997).
21. S. Gueron, K. Levit-Gurevich, Proc. Natl. Acad. Sci. U.S.A. **96**, 12240 (1999).
22. M.C. Lagomarsino, B. Bassetti, P. Jona, Eur. Phys. J. E **26**, 81 (2002); M.C. Lagomarsino, P. Jona, B. Bassetti, Phys. Rev. E **68**, 021908 (2003).
23. A. Vilfan, F. Jülicher, Phys. Rev. Lett. **96**, 058102 (2006).
24. P. Lenz, A. Ryskin, Phys. Biol. **3**, 285 (2006).
25. B. Guirao, J.-F. Joanny, Biophys. J. **92**, 1900 (2007).
26. J. Elgeti, G. Gompper, in preparation.
27. C. Goubault, P. Jop, M. Fermigier, J. Baudry, E. Bertrand, J. Bibette, Phys. Rev. Lett. **91**, 260802 (2003).
28. L. Cohen-Tannoudji, E. Bertrand, L. Bressy, C. Goubault, J. Baudry, J. Klein, J.F. Joanny, J. Bibette, Phys. Rev. Lett. **94**, 038301 (2005).
29. A. Koenig, P. Hébraud, C. Gosse, R. Dreyfus, J. Baudry, E. Bertrand, J. Bibette, Phys. Rev. Lett. **95**, 128301 (2005).
30. G. Taylor, Proc. R. Soc. London, Ser. A **209**, 447 (1951).
31. M. Reichert, H. Stark, Eur. Phys. J. E **17**, 493 (2005).
32. O. Kratky, G. Porod, Recl. Trav. Chim. Pays-Bas **68**, 1106 (1949).
33. J.R. Blake, Proc. Camb. Philos. Soc. **70**, 303 (1971).
34. J. Happel, H. Brenner, *Low Reynolds Number Hydrodynamics* (Noordhoff, Leyden, 1973).
35. L.D. Landau, E.M. Lifschitz, *Lehrbuch der Theoretischen Physik Band VII: Elastizitätstheorie* (Akademie Verlag, Berlin, 1991).
36. J.K.G. Dhont, *An Introduction to Dynamics of Colloids* (Elsevier, Amsterdam, 1996).
37. In our modeling, we use a center-to-center distance $3a$ of the particles in the filament (where a is the particle radius). In this case, the Rotne-Prager approximation deviates from the full multipole results of reference [38] by at most 5%. We checked this by using the program Hydrolib (see Ref. [39]).
38. B. Cichocki, B.U. Felderhof, K. Hinsen, E. Wajnryb, J. Blawdziewicz, J. Chem. Phys. **100**, 3780 (1994).
39. K. Hinsen, Comput. Phys. Commun. **88**, 327 (1995).
40. H.A. Lorentz, Zittingsverlag Akad. v. Wet. **5**, 168 (1896).
41. E.R. Dufresne, M. Todd, M.P. Brenner, D.G. Grier, Phys. Rev. Lett. **85**, 3317 (2000).
42. L. Durlofsky, J.F. Brady, G. Bossis, J. Fluid Mech. **180**, (1987).
43. G. Bossis, A. Meunier, J.D. Sherwood, Phys. Fluids A **3**, 1853 (1991).
44. J.W. Swan, J.F. Brady, Phys. Fluids **19**, 113306 (2007).
45. S. Melle, O.G. Calderón, M.A. Rubio, G.G. Fuller, Phys. Rev. E **68**, 041503 (2003).
46. A. Cēbers, I. Javaitis, Phys. Rev. E **69**, 021404 (2004).
47. Another obvious way of achieving a non-reciprocal motion of the superparamagnetic filament would be to vary the magnetic-field strength non-symmetrically during the actuation cycle. However, in our simulations we find that this method is less robust and effective.
48. J. Blake, J. Fluid Mech. **55**, 1 (1972).
49. Note that formally the induced flow along the y-direction should also depend on the force components F_{xi} and F_{zi}. Besides the fact that $F_{xi} = 0$ in our case, by symmetry the integrals of G_{yx}^{Blake} and G_{yz}^{Blake} over the (x, y)-plane vanish and additional contributions to equation (27) do not occur.
50. M. Fermigier, private communication.
51. G. Maret, private communication.
52. R.B. Jones, R. Kutteh, Phys. Chem. Chem. Phys. **1**, 2131 (1999).